Observation of an interfacial magnon-electron drag in a pyrochlore ferromagnet–heavy metal heterostructure

Avirup De,[1] Dharmalingam Prabhakaran,[2] and Sunil Nair[1]
[1]*Department of Physics, Indian Institute of Science Education and Research, Pune 411008, India*
[2]*Clarendon Laboratory, Department of Physics, University of Oxford, OX1 3PU, United Kingdom*

(Received 14 October 2022; revised 21 December 2024; accepted 31 January 2025; published 25 February 2025)

We report on how the deposition of a nonmagnetic metal on the surface of a ferromagnetic insulator can provide a sensitive, albeit indirect, means of measuring the magnon Hall effect. This is inferred from the thermoelectric potential that develops across the metal layer as a consequence of the transverse thermal Hall gradient. Moreover, a manifestation of magnon surface states is observed via the drag which the surface spin currents of the ferromagnet impose on the conduction electrons of the adjacent metallic layer. This electron-magnon interaction operates across the interface, and the polarity of the resultant drag voltage is determined by the spin Nernst angle of the metal layer.

DOI: 10.1103/PhysRevB.111.054435

I. INTRODUCTION

The electronic and thermodynamic properties of crystalline solids are often driven by wavelike collective excitations of quasiparticles associated with the lattice, spin, and charge degrees of freedom. A spin wave is one such entity within a magnet, and corresponds to a wavelike excitation of precessing spins within an ordered magnetic background. The quanta of these spin waves, or magnons, are characterized by a wave vector ($\vec{k}$) and frequency (ν), and provides a bosonic parallel of the oft-encountered electronic band structure in solids [1]. These bosonic quasiparticles also exhibit a Hall effect, and owing to their charge-neutral nature, this magnon Hall effect (MHE) cannot originate from the Lorentz force driven traditional Hall effect mechanisms. On the contrary, it is now widely acknowledged to be related to the Berry curvature of the magnon bands, suggesting that topology could play a important role in magnonic systems [2,3]. In experiments, the MHE is typically quantified by the transverse thermal Hall conductivity (K_{zx}), and involves the measurement of the transverse thermal gradient ($\frac{\partial T}{\partial x}$) arising due to the Berry curvature of magnon bands under the application of a longitudinal temperature gradient ($\frac{\partial T}{\partial z}$) and an orthogonal magnetic field (H) [4–11]. Prior experiments of MHE have relied on the use of external chip thermometers to estimate this transverse thermal gradient across the magnetic specimen [4–9]. Here we report on the use of a device geometry commonly used for the measurement of the spin Seebeck [12–14] or spin Nernst [15,16] effect for this purpose. This involves depositing a thin nonmagnetic metal (NM) on the specimen surface, and measuring the thermoelectric voltage driven by $\frac{\partial T}{\partial x}$, which develops across the length of the attached NM layer. In addition to an improved signal-to-noise ratio, this also allows us to observe a magnon-electron drag across the interface, with spin currents on the surface of the magnet manifesting itself as a measurable voltage across the NM layer.

II. EXPERIMENTAL DETAILS

We investigate $Y_2V_2O_7$/NM heterostructure devices made by depositing a thin (≈10 nm) NM layer (e.g., Pt, W, or Ta) on the crystal surfaces of the pyrochlore ferromagnet $Y_2V_2O_7$, using dc magnetron sputtering. This pyrochlore ferromagnetic insulator is characterized by the stacking of alternating kagome and triangular sublattices along the crystallographic [111] direction, and is predicted to possess a nontrivial magnon-band structure [17]. The absence of an inversion center in this structure results in a nonzero Dzyaloshinskii-Moriya interaction, which acts analogously to a vector potential [4], an essential factor for generating the nonvanishing Berry curvature of magnon bands [17]. This interaction deflects thermally driven magnon wave packets, leading to the emergence of a transverse thermal gradient due to magnon Hall transport. Thus, the application of a longitudinal temperature gradient ($\frac{\partial T}{\partial z}$) across the crystal induces a transverse temperature gradient ($\frac{\partial T}{\partial x}$) as a consequence of the thermal Hall effect of magnons. The transverse thermal gradient is subsequently detected via the thermoelectric response of an attached nonmagnetic metal (NM) layer. Measurements were performed by applying a longitudinal thermal gradient ($\frac{\partial T}{\partial z}$) across the crystal thickness (l_z), with an orthogonal magnetic field (H_y) oriented along the crystallographic [100] or [111] directions. In addition to detecting the thermal Hall effect of magnons arising from the magnon Hall effect (MHE), we also observed an interfacial electron-magnon drag when the field (H_y) was applied along the crystallographic [111] direction. Further details about the sample preparation and measurement protocols can be found in Appendix A.

III. RESULTS AND DISCUSSION

The MHE pertains to the generation of a transverse thermal gradient ($\frac{\partial T}{\partial x}$), due to the Hall transport of magnons in a direction orthogonal to both the applied magnetic field (H)

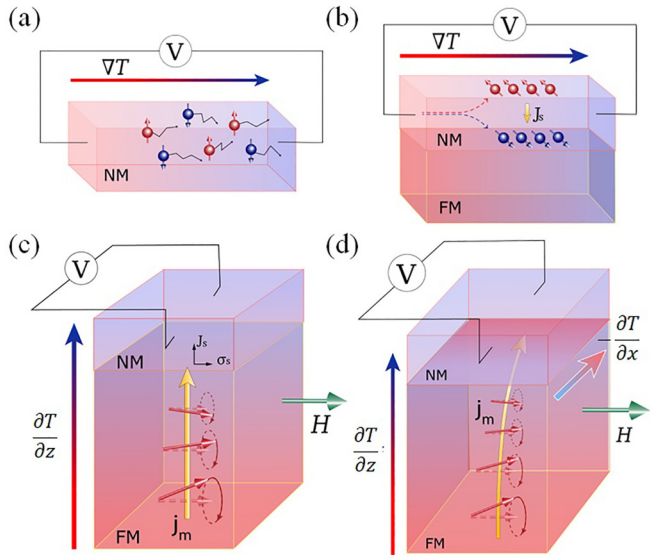

FIG. 1. Compendium of possible magnetothermal effects within our device architecture: (a) A nonmagnetic metal (NM) subjected to a temperature gradient (∇T) generates a thermoelectric voltage as a consequence of the Seebeck effect. If this nonmagnetic metal (NM) has large spin-orbit coupling, application of a thermal gradient (∇T) results in a transverse spin current (j_s) arising from the spin Nernst (-Ettingshuasen) effect, which is described in (b). When an insulating ferromagnet (FM) is placed adjacent to the NM, a correction to the thermoelectric voltage results as a function of the relative orientation of the spin polarization of the NM conduction electrons (at the interface) and the magnetization (of the FM layer). (c) Depicts the standard geometry utilized for measurements of the longitudinal spin Seebeck effect. Here the application of a temperature gradient across the FM-NM interface could result in a spin current (j_s) pumped into the NM, which can then manifest itself as a voltage via the inverse spin Hall effect. Our device architecture (d) comprises of a thin NM layer deposited on single-crystalline specimens of $Y_2V_2O_7$. Magnon wave packets traversing under the influence of an applied temperature gradient ($\frac{\partial T}{\partial z}$) are deflected owing to the finite Berry curvature of the magnon bands, resulting in a transverse temperature gradient ($\frac{\partial T}{\partial x}$). This transverse temperature gradient is measured via the thermoelectric response of the attached NM layer.

and the applied (longitudinal) thermal gradient ($\frac{\partial T}{\partial z}$). In our measurement geometry, the MHE signal is detected in terms of the thermoelectric voltage, driven by $\frac{\partial T}{\partial x}$ across the length of the attached NM layer. In addition to this thermoelectric voltage, we note that the $\frac{\partial T}{\partial x}$ could also generate an additional voltage due to the spin Nernst effect (SNE), as depicted in Fig. 1(b), if the attached NM layer possesses large spin-orbit interaction [15,16]. Since both the thermoelectric effect (TE) and SNE are driven by $\frac{\partial T}{\partial x}$, the total effect (TE+SNE) is considered as the MHE signal. However, since our measurement geometry is similar to that of the longitudinal spin Seebeck effect (LSSE) measurements, the MHE signal could be potentially contaminated by a parasitic voltage driven by LSSE if a net spin current is pumped through the interface into the attached NM layer, with the pumped spin current being further converted to an additional transverse electric voltage by means of the inverse spin Hall effect [12,14]. The possible contributory mechanisms are summarized in Figs. 1(a)–1(d). The voltage measured across the NM overlayer can be written as

$$V = \left[S + \Delta S_1 + \Delta S_2\left(1 - m_y^2\right)\right]\frac{\partial T}{\partial x} + V_{\mathrm{LSSE}}(T), \quad (1)$$

where the leading term S is the Seebeck coefficient of the NM layer, and $\Delta S_1, \Delta S_2$ are possible corrections to the Seebeck coefficient due to SNE. In the aforementioned Eq. (1), $\Delta S_1 = S\theta_{\mathrm{SH}}\theta_{\mathrm{SN}}\frac{2\lambda}{t_N}\tanh(\frac{t_N}{2\lambda})$, $\Delta S_2 = -S\theta_{\mathrm{SH}}\theta_{\mathrm{SN}}\frac{\lambda}{t_N}\mathrm{Re}\,\frac{2\lambda G\tanh^2\frac{t_N}{2\lambda}}{\sigma_{NM}+2\lambda G\coth\frac{t_N}{\lambda}}$, and $m_y = \mathbf{M}\cdot\hat{y}/|\mathbf{M}|$ [15,16]. Here, θ_{SH} and θ_{SN} are the spin Hall and spin Nernst angles of the attached NM, λ is the spin diffusion length inside the NM layer, t_N is the thickness of the NM layer, σ_{NM} is the electrical conductivity of the NM, G is the spin-mixing conductance at the interface, and $\mathbf{M}$ is the magnetization of the specimen. With the applied magnetic field oriented along the y direction, orthogonal to the measurement (x) direction, the contribution of ΔS_2 diminishes and ultimately vanishes as the magnetization reaches saturation. Furthermore, with $\Delta S_{1/2} \propto \theta_{\mathrm{SH}}\theta_{\mathrm{SN}}$, the contribution of the spin Nernst effect (SNE) is inferred to be several orders of magnitude lower than the leading Seebeck effect. The last term represents the effective spin Seebeck contribution, given by $V_{\mathrm{LSSE}} \propto \lambda\theta_{\mathrm{SH}}\tanh(\frac{t}{2\lambda})J_s$, where J_s is the net spin current pumped normal to the interface. Notably, the LSSE signal (V_{LSSE}) reverses its polarity depending on the sign of θ_{SH} of the NM [13,14,18]. In this study, the observed voltages across the attached NM layer are normalized to account for the sample dimensions and the applied thermal gradient, such that $V_{\mathrm{NM}} = \frac{V}{\frac{\partial T}{\partial z}} \times \frac{l_z}{l_x}$, where l_z is the thickness of the device and l_x the distance between voltage probes.

The $Y_2V_2O_7$ pyrochlore orders ferromagnetically at $T_C \approx 71$ K. The magnetic hysteresis as measured in the $H \parallel [100]$ direction of single crystalline $Y_2V_2O_7$ is depicted in Fig. 2(a). The magnetic field dependence of the measured thermoelectric voltage across the Pt and W layers in the $H \parallel [100]$ configuration is depicted in Figs. 2(b) and 2(c), respectively. The sample temperature during these measurements is kept at 60 K, which is below the paramagnetic-to-ferromagnetic transition temperature. The temperature dependence of the resistivity as measured in $Y_2V_2O_7$ [Fig. 2(d)] shows its insulating nature in the entire temperature regime of our interest. The temperature dependence of the magnetization measured in the $H \parallel [100]$ configuration is depicted in Fig. 2(e). Below the magnetic transition temperature, the MHE signal, represented by the thermoelectric voltage, is well resolved and exhibits clear dependencies on both the magnetic field [see Figs. 2(b) and 2(c)] and temperature [see Fig. 2(f)]. With the magnetic subunit being an insulator, the role of the ordinary and anomalous Nernst effects (ANE) in the measured thermoelectric voltage can be ruled out. The measured voltages having the same sign for both Pt and W layers, despite the opposite signs of their spin Hall angles (θ_{SH}) [19], as shown in Figs. 2(b) and 2(c), allows us to rule out a contribution of the LSSE. Hence, at applied fields being larger than the saturation field of $Y_2V_2O_7$, the measured voltage clearly comprises of the conventional thermoelectric effect in the NM layer alone, and is expected to be a direct measure of $\frac{\partial T}{\partial x}$ arising due to the MHE. The measured signal also scales linearly with the Seebeck coefficient of the attached metal layer (see

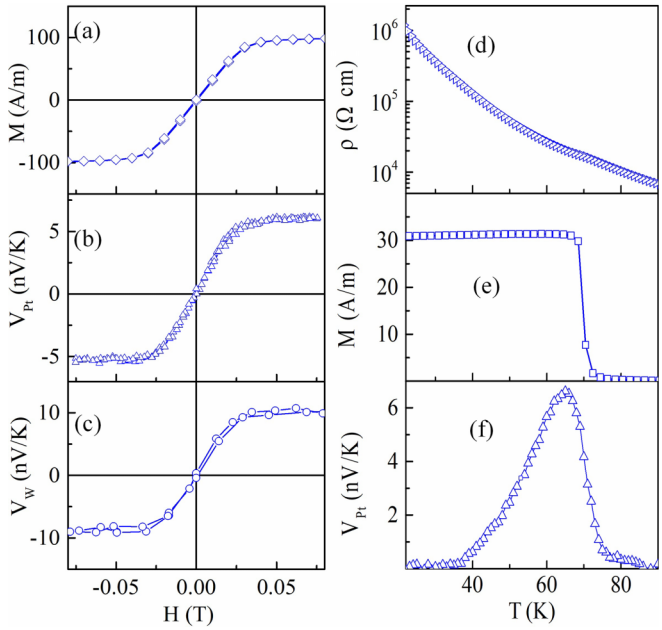

FIG. 2. This transverse gradient is measured via the thermoelectric response of the attached nm layer. The field dependence of this voltage with Pt and W layers is depicted in (a) and (b), respectively, with the magnetic field being applied along the [100] direction of $Y_2V_2O_7$. The measured voltage scales perfectly with the magnetization (c) as is expected for the MHE. The pyrochlore $Y_2V_2O_7$ is an insulator (d) with a paraferromagnetic phase transition at 71 K (e). The temperature dependence of the measured thermoelectric voltage as measured in the same configuration is depicted in (f).

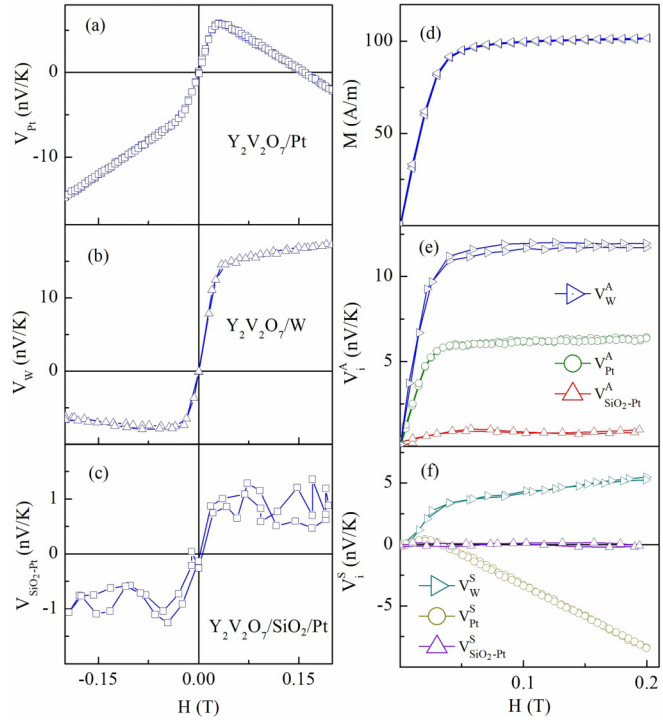

FIG. 3. A compendium of measurements on $Y_2V_2O_7$ in the $H \parallel [111]$ configuration. (a) Shows the magnetic field dependence of the thermoelectric voltage measured across a Pt layer at 60 K under an applied temperature gradient ($\frac{\partial T}{\partial z}$) of 10 K. Unlike the $H \parallel [100]$ configuration, the voltage in this configuration is not purely antisymmetric with respect to the applied field but includes an additional symmetric component. (b) Depicts the same measurement across a W overlayer, where the (albeit smaller) symmetric contribution is seen to reverse its sign. This symmetric component is notably absent (c) when a 10-nm SiO_2 buffer layer is inserted between the $Y_2V_2O_7$ crystal and the Pt layer. The magnetization as measured in the $H \parallel [111]$ direction is shown in (d). [(e),(f)] Present the magnetic field dependence of the antisymmetric and symmetric components of the transverse voltages measured across the Pt and W layers, respectively. The antisymmetric component arises from the MHE and is in consonance with the sample magnetization.

Appendix B for more details), which attests to the utility of this measurement methodology.

The temperature (T) dependence of this MHE signal would be determined by the T dependence of both the transverse thermal gradient $\frac{\partial T}{\partial x}(T)$ and the Seebeck coefficient of Pt. Since the latter is reported to have a smooth and nonvanishing functional form in the temperature regime of our experiments [20], the T dependence of the measured voltage is expected to mimic that of the MHE which determines the functional form of $\frac{\partial T}{\partial x}(T)$, and consequently that of the transverse thermal conductivity $K_{zx}(T)$. As seen in Fig. 2(f), this voltage rises below the onset of the magnetic transition, exhibits a peak at about 60 K, and then gradually decreases, in agreement with the thermal Hall conductivity expected to arise due to magnons. A significantly better signal-to-noise ratio in comparison to earlier reports [4,7] is observed, attesting to the utility of this device architecture in measurements of the MHE. Very recently, measurements utilizing a similar device geometry for the detection of the MHE have been reported [21], demonstrating that by employing a suitable metal overlayer, the MHE can be measured purely through (thermo)electric means.

The field dependence of the measured voltages in the $H \parallel [111]$ configuration as measured across a Pt and W layer is depicted in Figs. 3(a) and 3(b), respectively. The contrast with the field-dependent data obtained with $H \parallel [100]$ is significant since the antisymmetric voltage arising due to MHE is now seen to be superimposed with an additional *symmetric* component. This is evident in Figs. 3(e) and 3(f), where the field dependencies of the antisymmetric and symmetric components are individually depicted. The antisymmetric component of the measured voltage [shown in Fig. 3(e)] varies with the applied field and saturates in consonance with the magnetization [Fig. 3(d)]. Since the transverse heat flow due to the MHE reverses its direction upon reversing the magnetization of the magnetic subunit, $\frac{\partial T}{\partial x}$ is expected to be antisymmetric with respect to the applied magnetic field, implying that this component is consistent with the MHE. The symmetric component is also found to exhibit a significant field dependence, varying linearly with the magnitude of the applied field beyond the saturation magnetization, as shown in Fig. 3(f). In the low magnetic field regime, this could potentially arise due to magnetoresistive (MR) effects such as anisotropic magnetothermal resistance [22], spin-orbit magnetoresistance [23], and the spin Hall magnetoresistance [24,25]. However, all these MR effects necessarily saturate

with the magnetization of $Y_2V_2O_7$, implying that they cannot drive this symmetric component above the saturation magnetization fields. This advective symmetric contribution to the (otherwise diffusive) thermopower can potentially arise due to the magnon drag effect (MDE) [26–30]. In prior reports, the microscopic picture of MDE is described using the hydrodynamic [26,29] and relativistic spin motive force [27,28,30] approaches. The former models a magnetic metal as a two-component mixture of interacting magnons and electrons, whereas the latter relies on a spin-orbit interaction driven conversion of a magnon heat flux to an electric current [27,28,30]. Until now, MDE has been observed in magnetothermopower measurements of magnetic metals [28], and in magnon drag thermopile systems [29]. However, in principle, this effect could also be realized at the interface between a magnetic insulator and a normal metal. Here, $Y_2V_2O_7$ is a ferromagnetic insulator (FI), and the electrically conducting layer is the NM layer deposited over this FI crystal. Thus, the electron-magnon interaction necessarily has to occur *across* the interface, with the in-plane magnon current at the surface of $Y_2V_2O_7$ dragging the conduction electrons in the *adjacent* NM layer. We note that the phenomenon of interfacial phonon drag has been reported earlier in a Bi_2Te_3/Al_2O_3 device [31], where the electronic transport in the Bi_2Te_3 film is influenced by phonon transport in the substrate, with this interaction being operative at the interface. Similarly, an enhancement of the phonon drag at the interface was reported in a $LaAlO_3/SrTiO_3$ heterostructure [32], presumably owing to the confinement of the two-dimensional (2D) electron gas in this system. Our observations clearly point towards the magnon equivalent of such an interfacial effect. More recently, a theoretical investigation of a bilayer structure consisting of an antiferromagnetic insulator and a normal metal suggested that interfacial scattering processes facilitate the generation of a magnon current in an antiferromagnet, when an in-plane charge current is driven in the NM layer [33]. The interfacial origin of the observed symmetric component is further verified by inserting a (10-nm) SiO_2 buffer layer between the $Y_2V_2O_7$ crystal and the NM Pt layer. This is expected to decouple the surface magnons from the electrons in the metallic layer, while still retaining the (albeit diminished) transverse thermal gradient arising due to the thermal Hall. The magnetic field dependence of measurements performed in this configuration is depicted in Fig. 3(c) where the voltage is seen to be antisymmetric [shown in Fig. 3(e)] as is expected for the MHE, with the additional symmetric component being absent [as shown in Fig. 3(f)].

The electric current (j_d) due to the MDE can be expressed as [27,28,30]

$$\vec{j}_d = \frac{\sigma_\uparrow - \sigma_\downarrow}{e^2}\langle \vec{F}_i \rangle = \beta\sigma P_s \frac{\hbar}{2e}\frac{\vec{j}_m^q}{sD}. \tag{2}$$

Here, σ is the electronic conductivity at the interface ($\sigma = \sigma_\uparrow + \sigma_\downarrow$), with $\sigma_\downarrow$ and $\sigma_\uparrow$ being the conductivities with down- and up-spin polarizations, respectively, and $P_s = \frac{\sigma_\uparrow - \sigma_\downarrow}{\sigma}$ is the effective spin polarization. β is a dissipative spin-transfer torque parameter, e is the charge of an electron, s is the magnon density at the interface, and D is the spin stiffness. $\vec{j}_m^q = k_m \frac{\partial T}{\partial x}(H)$ is the magnon heat current, with k_m being the thermal conductivity of magnons at the interface. This electric current ($\vec{j}_d$) would be symmetric with respect to the applied field since both P_s and $\frac{\partial T}{\partial x}(H)$ reverse their polarities with $\vec{H}$. Furthermore, since the MDE depends on the spin polarization P_s of the itinerant electrons at the interface, this effect could potentially be tuned by the SNE of the attached nonmagnetic metal (NM) layer. This suggests that the polarity of the MDE signal, if present, would reverse its sign with the spin Nernst angle (θ_{SN}) of the NM layer. In addition, the magnetic field dependence of this drag is determined by that of the magnon heat flux $j_m^q(H)$, which can be expressed in terms of the quenching function [$L(y)$] [29]. This function varies approximately linearly with the strength of the effective magnetic field $|B_{\text{eff}}|$, in the low magnetic field limit. Since B_{eff} is determined by both the external magnetic field (H) and the sample magnetization (M), $L(y)$ is thus expected to vary linearly with $|H|$ above the saturation field of $Y_2V_2O_7$ (see Appendix C for more details). Figure 4(b) shows the magnetic field dependence of the symmetric magnon drag contribution as measured in the $H \parallel [111]$ configuration, where this linearity is clearly seen. Moreover, with the sign of θ_{SN} in Pt being opposite to that in W [16], the polarity of the symmetric component is also observed to reverse its sign when the Pt layer is replaced by W [see Figs. 3(f) and 4(b)], an observation that confirms MDE at the interface in the $H \parallel [111]$ configuration. This observation also suggest that a spin motive force at the interface plays a crucial role in the dragging

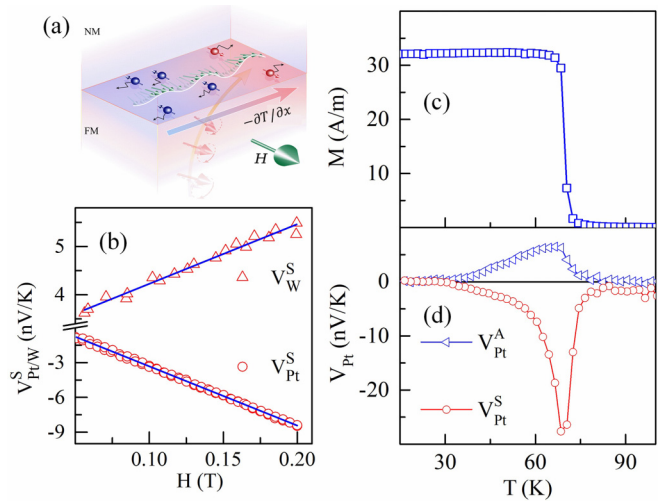

FIG. 4. The additional symmetric component in the thermoelectric voltage appears to arise from an interfacial magnon drag effect (a) where a surface spin current in the FM induces a charge current in the adjacent NM layer. The associated symmetric components, as measured in the Pt and W layers, above the saturation magnetization of $Y_2V_2O_7$ are shown in (b). The functional form of this symmetric voltage is derived from the linear magnetic field dependence of the quenching function $L(y)$, and the sign of its slope is determined by the θ_{SN} of the NM layer (see Appendix C for details). The temperature dependence of the magnetization as measured in the $H \parallel [111]$ configuration is shown in (c). The temperature dependence of both the asymmetric and symmetric components of the thermoelectric voltage as measured across a Pt layer in the $H \parallel [111]$ configuration is depicted in (d).

mechanism. Notably, this symmetric magnon drag contribution increases with a reduction in the thickness of the W layer due to the fact that θ_{SN} increases by lowering thicknesses of the W layer (see Appendix C). Figure 4(d) depicts the temperature dependence of both the antisymmetric (V_{Pt}^{A}) and the symmetric (V_{Pt}^{S}) components measured in this $H \parallel [111]$ configuration. It is observed that the symmetric component vanishes along with the antisymmetric component across the paramagnetic-to-ferromagnetic transition (T_c), which clearly suggests that the symmetric component is magnonic in origin. Since the magnon current at the interface vanishes along with the magnetization of the specimen at the transition temperature, it also reconfirms that the MDE is free from other spurious contributions like the phonon drag which is clearly absent in this case.

We speculate that the microscopic reason for the existence of a magnon drag contribution to the measured thermopower in the $H \parallel [111]$ configuration could be the nontrivial magnon topology in this class of materials. Prior theoretical calculations suggest that the magnon band structure of these pyrochlore ferromagnets comprises of four distinct bulk bands, with all of them possessing a nonvanishing Berry curvature [17]. This magnon band structure is also sensitive to the direction of the applied field, where a band gap between the first (lowest-energy) band and the second band exists as long as the magnetic field is *not within* the {100} plane of the crystal [17]. More importantly, a topologically protected surface magnon state is predicted to exist between the first and second bulk bands as long as this gap opening condition is satisfied. Since the magnon drag is linked to the momentum-transfer and spin-transfer processes [the β factor in Eq. (2)], an enhanced electron-magnon interaction at the interface [27,28,30] could be responsible for this additional voltage observed in the $H \parallel [111]$ configuration. Additional high field measurements which would open up a Zeeman gap in the magnon band structure could shed more light on both the observed magnon drag and the thermal Hall signals.

IV. CONCLUSIONS

In conclusion, we demonstrate an approach to measuring the MHE by depositing a thin layer of nonmagnetic metal on the surface of a pyrochlore ferromagnetic insulator $Y_2V_2O_7$. We utilize thermoelectric measurements to indirectly observe the MHE, and this method significantly enhances the signal-to-noise ratio. Our findings confirm that the thermoelectric voltage measured across the NM layer corresponds to the transverse thermal gradient induced by the MHE. Moreover, our data reveal a pronounced magnon-electron drag at the interface, observed as an additional voltage component in the thermoelectric voltage. The discovery of this interfacial magnon drag underscores the robust interaction between surface spin currents and conduction electrons across an interface, suggesting new avenues for advanced spintronic applications. Further examination of this interfacial phenomenon to optimize the magnon drag for practical applications will be essential. This not only advances the fundamental understanding of magnonic and spintronic phenomena, but also paves the way for the development of future magnonic devices utilizing magnon surface states for long-distance magnon transport and interfacial effects.

ACKNOWLEDGMENTS

A.D. acknowledges University Grants Commission (UGC) for a Senior Research Fellowship, and support from the DST Nanomission Thematic Unit Program (Grant No. SR/NM/TP13/2016). S.N. acknowledges support from a Science and Engineering Research Board grant (Grant No. SPR/2020/389) and the I-HUB Quantum Technology Foundation. D.P. acknowledges support from the Oxford-ShanghaiTech collaboration project and the UK Engineering and Physical Sciences Research Council (Grant No. EP/T028637/1).

APPENDIX A: MATERIALS AND METHODS

Polycrystalline $Y_2V_2O_7$ was synthesized using high-purity Y_2O_3, V_2O_3, and V_2O_5 starting chemicals. Powders were prepared using the solid-state reaction technique by two different routes: the precursor method and the vacuum sintering process. Precursors of YVO_4 and YVO_3 were mixed in a 1 : 1 molar ratio and feed rods were sintered under an argon atmosphere. In the second method, stoichiometric amounts of the starting chemicals were mixed and sintered under high vacuum at 1200 °C for 48 h with two intermediate grindings. Single crystals were grown using an optical floating zone furnace under argon atmosphere. Growth was carried out at a rate of 7–10 mm/h with feed and seed rods counter rotated at 25 rpm. These $Y_2V_2O_7$ crystals were then cut and polished into pieces, typically of dimensions of 3 mm × 2.5 mm × 1 mm, oriented along the [100] and [111] directions. The surface of the crystals used in our measurements were polished for extended periods at slow rotation speeds (≈6 h and 15 rpm) with 0.5-μm diamond paste using a precision polishing machine (EQ-Unipol-810). These specimens were then inspected using polarized light microscopy (Zeiss Lab A1, AXIO) to rule out cracks or other deformities on the crystal surface.

1. Measurement setup

Our measurement setup is housed in a closed-cycle refrigerator mated with an electromagnet. The sample is mounted in a custom-made sample holder by sandwiching it between two copper blocks. In addition to a strip heater mounted at the cold head of the refrigerator, two cartridge heaters are also attached to the sample holder to control both the thermal gradient ($\frac{\partial T}{\partial z}$) across the sample thickness ($l_z \approx 1$ mm) and the average temperature of the sample. The temperatures at the opposite ends of the sample are measured by two calibrated Cernox sensors attached near the sample edges The sample temperature is maintained by two-stage heating, with the strip heater maintaining the base temperature, and the cartridge heaters being operated to fine tune the temperature gradient. The geometry of the holder (Fig. 5) is such that the applied thermal gradient is always orthogonal to the rotation plane of the magnetic field. For electrical isolation between the sample and the holder, the sample ends of both the copper blocks are covered by using sapphire plates. Temperature is controlled

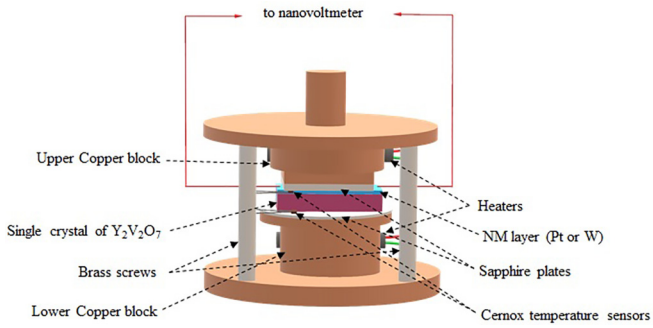

FIG. 5. A schematic of the sample holder used in our measurements (not to scale). This holder is attached to the cold head of a closed-cycle refrigerator, and placed between the poles of a laboratory electromagnet.

and monitored using a Lakeshore 336 cryogenic temperature controller, and the signal voltages are measured using a Keithley 2182A nanovoltmeter. The whole setup (including the nanovoltmeter) is housed in a dual (nested) Faraday cage to reduce the effective noise floor.

2. Measurement methodology

The MHE is directly linked to the generation of a transverse thermal gradient ($\frac{\partial T}{\partial x}$) under the application of an external longitudinal thermal gradient ($\frac{\partial T}{\partial z}$), a phenomenon also known as thermal Hall effect of magnon (THEM). To detect this MHE signal, we deposited a nonmagnetic metal (NM), such as Pt, W, or Ta, on the polished crystal surface, enabling the measurement of thermoelectric voltages driven by ($\frac{\partial T}{\partial x}$). This was done using dc magnetron sputtering, and the thickness of the NM layer was approximately kept at 10 nm. The MHE signal was quantified by measuring the voltage (V) along the length of the NM layer in the x direction, which is transverse to both the applied thermal gradient ($\frac{\partial T}{\partial z}$) and the magnetic field. The sample was mounted at the sample holder (attached at the cold head of the CCR), where it was sandwiched between two rectangular copper blocks. The applied thermal gradient ($\frac{\partial T}{\partial z}$), as well as the average sample temperature T, was controlled by two programmable instrument devices (PID) controlled heaters, and the temperatures were measured by two calibrated Cernox temperature sensors. Apiezon N grease and sapphire substrates were also used in-between the sample and the copper blocks for better thermal connection and electrical isolation. In our case, $\delta T_{\rm app} = T_2 - T_1$ is the applied temperature difference across the thickness of the crystal (l_z), where T_1 and T_2 are the measured temperatures at the opposite surfaces of the crystal. Thus, the applied thermal gradient is approximated as $\frac{\partial T}{\partial z} = \delta T_{\rm app}/l_z$. Similarly, the average sample temperature is determined as $T = \frac{1}{2}(T_1 + T_2)$. The sample holder was designed such that the applied magnetic field (H) always remains orthogonal to the applied thermal gradient ($\frac{\partial T}{\partial z}$), and the MHE signal was measured along the x direction, which is orthogonal to both the external H (the y direction) and the applied $\frac{\partial T}{\partial z}$ (the z direction).

H-dependent measurements are conducted by varying the applied magnetic field (H) while maintaining constant values for both the applied thermal gradient ($\frac{\partial T}{\partial z}$) and the average temperature (T). Similarly, *T-dependent measurements* are performed by varying T from 18 to 100 K, keeping both $\frac{\partial T}{\partial z}$ and H fixed. To isolate the MHE and MDE signals, the transverse voltage measured at $H = 0$, referred to as the background voltage [$V(0)$], is subtracted from the measured transverse voltages.

We note that the MHE is purely antisymmetric in nature, meaning it reverses its polarity with the applied magnetic field. In contrast, the MDE is symmetric, whose polarity remains invariant with the direction of the applied magnetic field. Here, the symmetric ($V^S_{\rm NM}$) and antisymmetric ($V^A_{\rm NM}$) components of the measured transverse voltages are determined as

$$V^S_{\rm NM}(H) = \tfrac{1}{2}[V_{\rm NM}(+H) + V_{\rm NM}(-H)],$$
$$V^A_{\rm NM}(H) = \tfrac{1}{2}[V_{\rm NM}(+H) - V_{\rm NM}(-H)]. \quad \text{(A1)}$$

APPENDIX B: ADDITIONAL INFORMATION ON THE MHE SIGNALS

The structural, magnetic, and electronic properties of $Y_2V_2O_7$ are reported to be similar to the more extensively investigated $Lu_2V_2O_7$ system [34–36]. Since $Lu_2V_2O_7$ is reported to exhibit significant MHE [4,7,37], a similar effect is also expected in $Y_2V_2O_7$. The absence of an inversion center in the unit-cell structure of these pyrochlore ferromagnets leads to a nonzero Dzyaloshinskii-Moriya interaction, which mimics the role of a vector potential [4]. This interaction is an essential ingredient for the nonvanishing Berry curvature of the magnon bands [17]. Consequently, it deflects thermally driven magnon wave packets, resulting in a transverse thermal gradient ($\frac{\partial T}{\partial x}$) due to magnon Hall transport. Theoretically, the associated transverse thermal conductivity (K_{zx}) of such a pyrochlore ferromagnet can be expressed as $K_{zx} = 2T\sum_n \int_{\rm BZ} \frac{d^3k}{(2\pi)^3} c_2[\rho_n(\mathbf{k})]\Omega_{n,z}(\mathbf{k})$, with $c_2(\rho) = (1+\rho)(\log\frac{1+\rho}{\rho})^2 - (\log\rho) - 2Li(-\rho)$, and the local Berry curvature of the nth magnon band $\Omega_{n,z}(\mathbf{k}) = {\rm Im}\langle\frac{\partial\psi_n(k)}{\partial k_x}|\frac{\partial\psi_n(k)}{\partial k_y}\rangle$ [7,11,38,39]. Here, n is the index that describes the discrete energy level of the magnon bands, ρ is the Bose-Einstein distribution function of magnons, and $\psi_n(\mathbf{k})$ is the wave function of magnons at the nth energy band having momentum $\mathbf{k}$. Thus, the MHE signal arises as a consequence of the additive contribution of individual magnon bands having nonvanishing Berry curvatures. The c_2 function, determined by the magnon population at a band, plays an important role in determining the effective contribution of each band, and it has been suggested that the contributions of magnons from higher-energy bands are significantly suppressed at low temperatures due to this function [40]. As the temperature is increased, bands of higher energies become occupied and start contributing more significantly to the MHE. It has been predicted that the magnon-band structure of a pyrochlore ferromagnet comprises of four distinct bulk bands of magnons, with all of them possessing nonvanishing Berry curvature [17]. The temperature dependence of the MHE signals $V^A_{\rm Pt/W}(T)$, shown in Fig. 6, shows that it becomes negligibly small at temperatures below $T^*(\approx 30$ K). It suggests that the role of occupied magnons bands at these low temperatures is

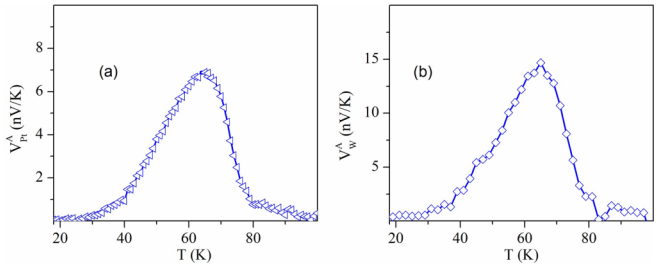

FIG. 6. Temperature dependence of the MHE signals, measured by the attached (a) Pt layer, (b) W layer. Here, both the applied H and $\delta T_{\rm app}$ are kept fixed at 0.2 T and 10 K, respectively. All the MHE signals are measured under the $H \parallel [111]$ configuration.

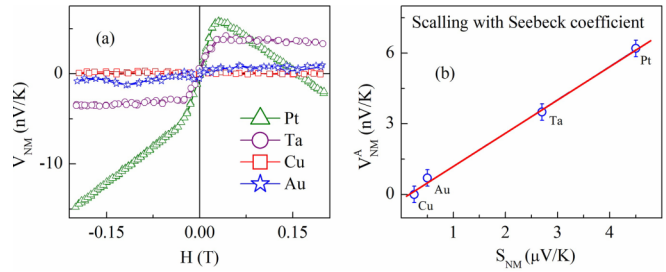

FIG. 7. (a) Shows that magnetic field dependence of the total voltages, as measured in the $H \parallel [111]$ configuration at an average sample temperature of 60 K. The antisymmetric component [shown in (b)] of the measured signal scales linearly with the Seebeck coefficients of the attached NM layers.

insignificant in comparison to that of the higher-energy bands. With increasing temperature, magnon at higher-energy bands starts contributing to MHE. We observe that the MHE signal monotonically increases with the sample temperature, and achieves its maximum value as the temperature reaches close to the ferromagnetic-to-paramagnetic transition temperature ($T_c \approx 70$ K). We speculate that this is a consequence of the disruption of the ferromagnetic order within the crystal, when the high-temperature end of the crystal reaches T_c. Since the ferromagnetic state of the crystal is destabilized, the signal starts decreasing with further increasing the temperature, and it vanishes when the sample completely enters into the paramagnetic phase. In prior experimental reports, the MHE has been analyzed under the assumption that the lowest magnon band predominantly determines the MHE signal [4,7]. However, such an assumption also leads to an overwhelming value of the $\frac{D}{J}$ ratio [40], where D and J are the strengths of the Dzyaloshinskii-Moriya interaction and the nearest-neighbor exchange interaction of the pyrochlore ferromagnet, respectively. Moreover, the functional form of $K_{zx}(T)$, derived from the lowest magnon band, shows a monotonically increasing function of temperature [7].

In our measurements, the MHE signal ($\frac{\partial T}{\partial x}$) is detected in terms of the thermoelectric effect (TE) of the attached NM layer (Pt or W). In addition to this TE, SNE could also contribute by an additional voltage, if the attached NM layer possesses large spin-orbit interaction [15,16]. In the case of Pt, $\theta_{\rm SH} \approx 0.1$ [19], and $\theta_{\rm SN} \approx -0.2$ [15]. Thus, the contribution of SNE [through the ΔS_1 and ΔS_2 terms in Eq. (2)] to MHE is expected to be a couple of orders smaller than the contribution of TE [first term in Eq. (2)]. Furthermore, the contribution of ΔS_2 vanishes when the magnetization is saturated in the y direction. Thus, the $V_{\rm Pt}$ signal is primarily driven by the conventional TE of the Pt layer alone, with the functional form of $V_{\rm Pt}(T)$ being determined by the temperature dependence of both the $\frac{\partial T}{\partial x}$ and the Seebeck coefficient of Pt ($S_{\rm Pt}$). With the $S_{\rm Pt}(T)$ being reported to show a smooth and nonvanishing functional form in the whole temperature regime of our experiments [20], the temperature dependence of the measured voltage is expected to mimic that of the MHE characterized by the transverse thermal conductivity (K_{zx}). In the case of W, $\theta_{\rm SH} \approx -0.14$ [19] and $\theta_{\rm SN}$ takes a value between 0.22 to 0.42 [16], implying that the $V_{\rm W}(T)$ signal is also mostly driven by the TE effect of the attached W layer. For any NM layer having lower spin-orbit interaction, the effect of SNE would be further reduced. Thus, the observed antisymmetric component of the measured voltage predominantly arises from thermoelectric effects that scale with the Seebeck coefficient of the attached layer. In order to verify that our measurement protocol, we check whether the antisymmetric component scale linearly with the Seebeck coefficient of the attached NM. We performed measurements by depositing different NM layers (NM $\equiv$ Pt, Au, Ta, and Cu), with the thickness of the NM layer being kept constant at $\approx$10 nm. Since the attracted NM layer also introduces a shunting path for heat current, it might reduce the effective $\frac{\partial T}{\partial x}$. However, we have estimated that such reduction is negligible as the thickness of the NM layer are kept very small ($\approx$10 nm). In order to check the scaling of the measured signals, we have relied on the reported values of Seebeck coefficients of Pt, Ta, Au, and Cu at 60 K. Prior reports suggest that the Seebeck coefficient of Pt ($S_{\rm Pt}$), Ta ($S_{\rm Ta}$), Au ($S_{\rm Au}$), and Cu ($S_{\rm Cu}$) are approximately 4.5 μV/K [41–43], 2.7 μV/K [44], 0.5 μV/K [45], and 0.25 μV/K [45], respectively. Figure 7(a) shows the magnetic field dependence of the total voltages measured in the $H \parallel [111]$ configuration at 60 K. Figure 7(b) shows that the antisymmetric component ($V^A_{\rm NM}$) of the measured signals in the saturation magnetization regime scales with the Seebeck coefficient ($S_{\rm NM}$) of the attached NM, confirming that the measured signals primarily stem from the thermoelectric effect, and that other parasitic voltages can be safely ignored. Consequently, the observed scaling behavior of the antisymmetric component validates our measurement methodology. The ($V^A_{\rm NM}$) is also observed to vary linearly with the applied thermal gradient (as shown in Fig. 8). This observation suggests that ($\frac{\partial T}{\partial x}$) varies linearly with the applied thermal gradient ($\frac{\partial T}{\partial z}$). Consequently, any heat loss through the thin Pt layer, which might reduce the transverse thermal gradient ($\frac{\partial T}{\partial x}$), is inferred to be negligibly small.

APPENDIX C: NOTES ON THE MAGNON DRAG EFFECT

Magnon drag effect (MDE) pertains to the flow of electrons dragged by the magnon current in a material system [27–30,46,47]. In earlier reports, MDE was understood in terms of an additional contribution to the thermopower in a ferromagnetic metal, where the electrons and magnons flow not only independently but also by dragging each other under the application of an external temperature gradient

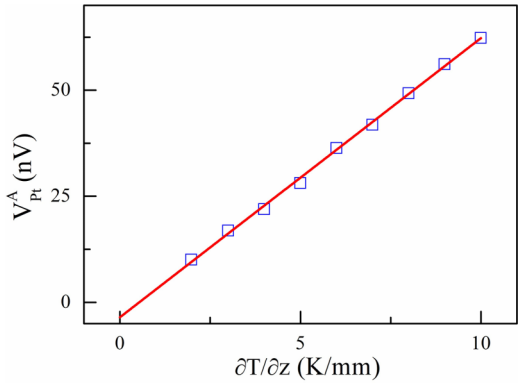

FIG. 8. The applied thermal gradient $[(\frac{\partial T}{\partial x})]$ dependence of the raw antisymmetric component of the tranverse voltage measured Pt layer in the $H \parallel [111]$ configuration at 60 K.

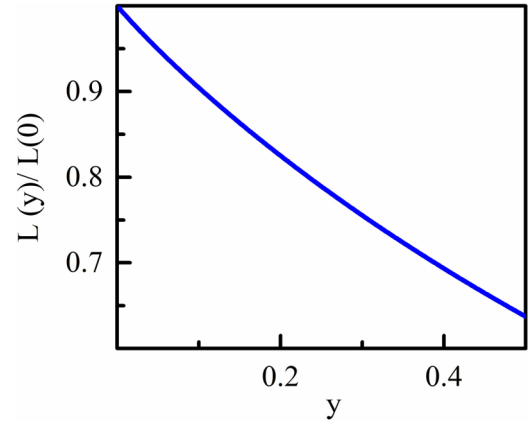

FIG. 9. Normalized quenching function $\frac{L(y)}{L(o)}$, calculated by numerical integration. $L(y)$ determines the role of magnetic field on the MDE beyond the saturation magnetization.

[26,28,30,48]. More recently, Costache and coworkers have experimentally verified the existence of MDE by eliminating the possible contribution of phonon drag effect, and confirmed that such MDE could vary linearly with the applied H beyond the saturation magnetization of the specimen [29].

In the $Y_2V_2O_7$/NM bilayers, we invoke MDE in order to explain the linearly varying symmetric component $[V^S_{NM}(H)]$ of the total transverse voltage $[V_{NM}(H)]$ measured in the $H \parallel [111]$ configuration. Since the observed $V^S_{NM}(H)$ arises additively along with $V^A_{NM}(H)$, the invoked MDE is thought to exist alongside the aforementioned TE and SNE. The microscopic mechanism of MDE has been theoretically described in terms of the spin motive force, where the magnon current exerts a dragging force to the conduction electrons that depends on the spin polarization of those electrons [28,30,46]. In our case, an in-plane magnon current at the interface could drag the conduction electrons along the length of the attached NM layer, with the polarization of these dragged electrons being determined by the SNE of that NM layer. This *interfacial magnon drag*, akin to the previously discovered interfacial phonon drag effect [49,50], is the key to inferring on the presence of magnon-driven surface spin currents in the $Y_2V_2O_7$ system.

1. Possible magnon currents and the associated dragging effects at the interface

In our case, two types of magnon currents could possibly exist at the interface. The first one is j^f_m, a small counterpart of the magnon Hall current flowing at the interface. The second is j^r_m, originating from the $\frac{\partial T}{\partial x}$ at the interface via the spin Seebeck effect. Thus, $j^r_m = S_m \frac{\partial T}{\partial x}$, where S_m is spin Seebeck coefficient. Since $\frac{\partial T}{\partial x}$ is generated by MHE, the direction of j^r_m would have the opposite in direction to that of j^f_m. The effective magnon current at the interface would be

$$j^{\text{eff}}_m = j^f_m - j^r_m. \tag{C1}$$

If j_d is the dragged electric current due to j^{eff}_m, its functional form could be written as [27,28,30,46,47]

$$j_d = -\beta\sigma P_s \frac{\hbar}{2e}\frac{j^q_m}{sD}, \tag{C2}$$

where β is the dissipative spin-transfer torque parameter; σ is the electronic conductivity at the interface ($\sigma = \sigma_\uparrow + \sigma_\uparrow$, where $\sigma_\downarrow$ and $\sigma_\uparrow$ are the conductivities with up- and down-spin polarizations, respectively); $P_s = \frac{\sigma_\uparrow - \sigma_\downarrow}{\sigma}$ is the spin polarization of conduction electrons at the interface (in our case, P_s is determined by the spin accumulation driven by the SNE at interface, and thus saturates with the specimen's magnetization); e is the charge of an electron; s is the magnon density at the interface; D is the spin stiffness; and j^q_m is the magnon heat current carried by j^{eff}_m at the interface. $j^q_m(H)$ can be written as [26,28,29]

$$j^q_m = \frac{j^{\text{eff}}_m}{ne}\frac{(k_BT)^{5/2}}{6\pi^2 D^{3/2}}L(y), \tag{C3}$$

where n is the density of the conduction electrons at the interface, T is the temperature, k_B is the Boltzmann constant, and $L(y)$ is called the "quenching function." By considering a quadratic magnon dispersion (which is a reasonable estimate because of the integration in the entire momentum space [29]), the functional form of $L(y)$ can be written as

$$L(y) = \int_0^\infty x^{3/2}(x+y)\frac{e^{x+y}}{(e^{x+y}-1)^2}\,dx, \tag{C4}$$

where $x = \frac{Dq^2}{k_BT}$ and $y = \frac{g\mu_B B}{k_BT}$. Here, q, g, μ_B, and B are the magnon's wave vector, Lande g factor, the Bohr magneton, and total magnetic field, respectively [26,29]. Thus, Eqs. (7) and (8) suggest that the magnetic field dependence of the associated MDE is expected to vary with $L(y)$ in the saturation magnetization regime.

We numerically integrate $L(y)$ as depicted in Fig. 9, where the y dependence of $L(y)/L(0)$ [with $L(0) = 4.45$] is shown. In agreement with prior papers [29], this numerical integration suggests that $L(y)$ varies approximately linearly at low values of y (typically $y \leqslant 0.1$). In our case, since the maximum magnetic field is only 0.2 T, the maximum value of y accessed in our measurements would be less than 0.1. Furthermore, since $y = \frac{g\mu_B H}{k_BT}$, $L(y)$ could be expressed as $L(H)$ by keeping the temperature fixed. Thus, with $L(H)$ decreasing linearly with H from its maximum value $L(0)$, the functional form of $L(H)$

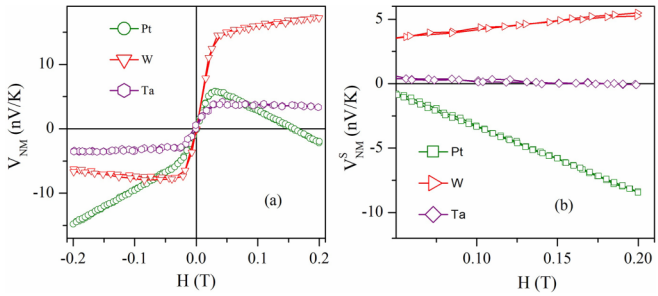

FIG. 10. (a) Shows the transverse signals measured by Pt, W, and Ta layers in the in the $H \parallel [111]$ configuration. (b) Illustrates the symmetric components of the measured signals in the saturation magnetization regime.

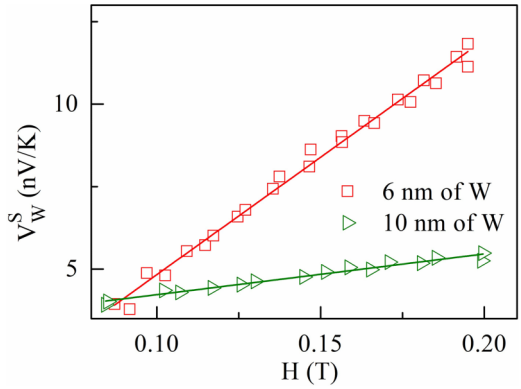

FIG. 11. Magnetic field dependence of symmetric component in the saturated magnetization regime, as measured by W layer of thickness of both 6 and 10 nm. Owing to the increased spin Nernst angle to β phase of the W, an increased dragging effect is observed.

could be formulated as $L(H) = L(0) - \alpha H$, where α is the slope of the linear function.

2. The magnetic field dependence of the dragged electric current

Above the saturation magnetization, the dragged electric current can be expressed as $[j_d(H) - j_d(H_s)]$, where H_s is the external magnetic field at which the magnetization gets saturated. Thus, by utilizing Eqs. (7)–(9), the magnetic field dependence of $[j_d(H) - j(H_s)]$ is determined by the quenching function as $[L(H) - L(H_s)]$. Mathematically, this can be described as

$$\begin{aligned}[j_d(H) - j_d(H_s)] &= \frac{\hbar\beta\sigma P_s}{2esD}\left[j_m^q(H) - j_m^q(H_s)\right] \\ &= \frac{\hbar\beta\sigma P_s}{2esD}\frac{j_m^{\text{eff}}}{ne}\frac{(k_BT)^{5/2}}{6\pi^2D^{3/2}}[L(H) - L(H_s)] \\ &= \eta P_s[L(H) - L(H_s)] \\ &= -\alpha\eta P_s H + \text{const}, \end{aligned} \tag{C5}$$

where $\eta = \frac{\hbar\beta\sigma}{2esD}\frac{j_m^{\text{eff}}}{ne}\frac{(k_BT)^{5/2}}{6\pi^2D^{3/2}}$. Since both the j_m^f and the j_m^r are driven by the MHE, both j_m^f and j_m^r saturate with magnetization, implying that j_m^{eff} also saturates with magnetization. Thus, η becomes a constant factor at a fixed temperature in the saturation magnetization regime. Equation (8) clearly shows that the magnon drag varies linearly with the applied H above the saturation magnetization, where the slope is determined by the sign of P_s. With the P_s being determined by the SNE, its polarity depends on the θ_{SN} of the attached NM layer. The fact that θ_{SN} of Pt is opposite in sign to that of W [15,16,51] also explains why the slope of $V^S_{\text{NM}}(H)$ in the saturation magnetization regime is observed to change its sign when the Pt layer is replaced by the W layer [see Fig. 4(b) in the main text, and Fig. 10(b)]. Aside from such linear functional form of MDE, its symmetric nature is also expected because of the fact that both the P_s and J_m^{eff} reverse their polarities on reversing the direction of H. To reconfirm the interfacial MDE, we conducted additional measurements by depositing a Ta layer on the $Y_2V_2O_7$ crystal. The small spin Nernst angle (θ_{SN}) of Ta [51] results in minimal spin accumulation at the interface, significantly suppressing the drag effect. This suppression is evident in Fig. 10(b), where the symmetric component measured with the Ta layer is substantially reduced compared to those for Pt and W layers. Figure 10(a) illustrates the measured transverse voltages by attaching Pt, W, and Ta layers in the $H \parallel [111]$ configuration. Despite its small θ_{SN} [51], Ta exhibits a notable spin Hall angle ($\theta_{\text{SH}} \approx -0.071$) [19], with a polarity opposite to that of Pt. Interestingly, the polarity of V_{Ta} aligns with the antisymmetric component of V_{Pt}, reaffirming that the observed signals are not influenced by contributions from the longitudinal spin Seebeck effect (LSSE). Below the saturation magnetization field, the drag effect depends on the H dependence of both $j^{\text{eff}}m$ and $\frac{\partial T}{\partial x}$, while the quenching function $L(y)$ varies linearly with the total magnetic field, which is the sum of the specimen's magnetization (M) and the applied field (H). Although quantifying the individual contributions to the symmetric component $V^S_{\text{NM}}(H)$ in the low-field regime is beyond the scope of this work, we emphasize that j_m^{eff} and $\frac{\partial T}{\partial x}$ remain nearly constant in the saturation magnetization regime. This invariance simplifies the analysis of $V^S_{\text{NM}}(H)$ *above* the saturation field, enabling a straightforward observation of the linear variation in the symmetric component, whose polarity is determined by the spin Nernst angle (θ_{SN}) of the attached NM layer.

In Table I, we summarize the characteristics of the observed signals above the saturation magnetization of $Y_2V_2O_7$. For the MHE, the sign of the measured antisymmetric component remains independent of the spin Hall angle (θSH) and spin Nernst angle (θSN) of the attached NM layer. In contrast, for the MDE, the magnon drag voltage is governed by the spin polarization of the conduction electrons at the interface, thereby involving the SNE of the attached NM layer. Consequently, the observed MDE signals, inferred from the symmetric components, are found to vary commensurately with the θ_{SN} of the attached NM layer. This observation provides direct evidence for MDE in the $H \parallel [111]$ configuration.

We have also performed measurements by using W layers of different thicknesses (10 and 6 nm). As the relative phase fractions of the β and α phases of W depend on the film thickness, it affects the spin Nernst angle of the W layer significantly. Prior reports show that in W films of lower thickness, the fraction of β phase is enhanced, which then commensurately increases the spin Nernst angle [51]. As is shown in Fig. 11, our measurement with a 6-nm-thick W

TABLE I. Summary of MHE and MDE signals obtained with different NM layers.

Observation and reports	Pt	W	Ta
Spin Hall angle (θ_{SH})	≈0.1 [19]	≈−0.14 [19]	≈−0.071 [19]
Spin Nernst angle (θ_{SN})	−0.2 [15,16]	$0.22 \leqslant \theta_{SN} \leqslant 0.42$ [16,51]	Negligible [51]
Antisymmetric component $\left(V^{A}_{NM}\right)$	Polarity commensurate with the magnetization	Polarity commensurate with the magnetization	Polarity commensurate with the magnetization
Spin accumulation at the interface due to SNE	Significant, and negative spin polarization	Significant, and positive spin polarization	Insignificant, due to negligible θ_{SN}
Symmetric component $\left(V^{S}_{NM}\right)$	Significant dragging, with negative slope	Significant dragging, with positive slope	Insignificant, due to insignificant spin accumulation at the interface

layer shows a stronger dragging effect in comparison to that observed in a 10-nm W layer.

3. On ruling out phonon drag

Since a phonon flow due to the magnon Hall induced heat gradient ($\frac{\partial T}{\partial x}$) cannot be ruled out, it is important to consider whether the phonon drag effect [31,32,49,50] can result in the observed symmetric component (V^{S}_{NM}). It is to be noted that the slope of the linearly varying symmetric component [$V^{S}_{Pt/W}(H)$] in the saturated magnetization regime is found to change its polarity when the Pt- is replaced by the W layer, an observation that can not be explained by phonon drag effect. In addition, the magnetic field dependence of a phonon dragged voltage is expected to be commensurate with the direction of generated thermal gradients, implying that it would be antisymmetric in nature and would also saturate with the $\frac{\partial T(H)}{\partial x}$. This indicates that the phonon drag contribution can be effectively ruled out in our case.

[1] N. P. Armitage, E. J. Mele, and A. Vishwanath, Weyl and Dirac semimetals in three-dimensional solids, Rev. Mod. Phys. **90**, 015001 (2018).

[2] P. A. McClarty, Topological magnons: A review, Annu. Rev. Condens. Matter Phys. **13**, 171 (2022).

[3] C.-K. Chiu, J. C. Y. Teo, A. P. Schnyder, and S. Ryu, Classification of topological quantum matter with symmetries, Rev. Mod. Phys. **88**, 035005 (2016).

[4] Y. Onose, T. Ideue, H. Katsura, Y. Shiomi, N. Nagaosa, and Y. Tokura, Observation of the magnon Hall effect, Science **329**, 297 (2010).

[5] D. Watanabe, K. Sugii, M. Shimozawa, Y. Suzuki, T. Yajima, H. Ishikawa, Z. Hiroi, T. Shibauchi, Y. Matsuda, and M. Yamashita, Emergence of nontrivial magnetic excitations in a spin-liquid state of kagomé volborthite, Proc. Natl. Acad. Sci. USA **113**, 8653 (2016).

[6] M. Hirschberger, J. W. Krizan, R. J. Cava, and N. P. Ong, Large thermal Hall conductivity of neutral spin excitations in a frustrated quantum magnet, Science **348**, 106 (2015).

[7] T. Ideue, Y. Onose, H. Katsura, Y. Shiomi, S. Ishiwata, N. Nagaosa, and Y. Tokura, Effect of lattice geometry on magnon Hall effect in ferromagnetic insulators, Phys. Rev. B **85**, 134411 (2012).

[8] Y. Kasahara, K. Sugii, T. Ohnishi, M. Shimozawa, M. Yamashita, N. Kurita, H. Tanaka, J. Nasu, Y. Motome, T. Shibauchi, and Y. Matsuda, Unusual thermal Hall effect in a Kitaev spin liquid candidate α-$RuCl_3$, Phys. Rev. Lett. **120**, 217205 (2018).

[9] M. Hirschberger, R. Chisnell, Y. S. Lee, and N. P. Ong, Thermal Hall effect of spin excitations in a kagome magnet, Phys. Rev. Lett. **115**, 106603 (2015).

[10] H. Katsura, N. Nagaosa, and P. A. Lee, Theory of the thermal Hall effect in quantum magnets, Phys. Rev. Lett. **104**, 066403 (2010).

[11] R. Matsumoto and S. Murakami, Theoretical prediction of a rotating magnon wave packet in ferromagnets, Phys. Rev. Lett. **106**, 197202 (2011).

[12] J. Xiao, G. E. W. Bauer, K.-C. Uchida, E. Saitoh, and S. Maekawa, Theory of magnon-driven spin Seebeck effect, Phys. Rev. B **81**, 214418 (2010).

[13] K. Uchida, J. Xiao, H. Adachi, J. Ohe, S. Takahashi, J. Ieda, T. Ota, Y. Kajiwara, H. Umezawa, H. Kawai, G. E. W. Bauer, S. Maekawa, and E. Saitoh, Spin Seebeck insulator, Nat. Mater. **9**, 894 (2010).

[14] A. De, A. Ghosh, R. Mandal, S. Ogale, and S. Nair, Temperature dependence of the spin Seebeck effect in a mixed valent manganite, Phys. Rev. Lett. **124**, 017203 (2020).

[15] S. Meyer, Y.-T. Chen, S. Wimmer, M. Althammer, T. Wimmer, R. Schlitz, S. Geprägs, H. Huebl, D. Ködderitzsch, H. Ebert *et al.*, Observation of the spin Nernst effect, Nat. Mater. **16**, 977 (2017).

[16] D.-J. Kim, C.-Y. Jeon, J.-G. Choi, J. W. Lee, S. Surabhi, J.-R. Jeong, K.-J. Lee, and B.-G. Park, Observation of transverse spin Nernst magnetoresistance induced by thermal spin current in ferromagnet/non-magnet bilayers, Nat. Commun. **8**, 1400 (2017).

[17] A. Mook, J. Henk, and I. Mertig, Tunable magnon Weyl points in ferromagnetic pyrochlores, Phys. Rev. Lett. **117**, 157204 (2016).

[18] S. M. Rezende, R. L. Rodríguez-Suárez, R. O. Cunha, A. R. Rodrigues, F. L. A. Machado, G. A. Fonseca Guerra, J. C. Lopez Ortiz, and A. Azevedo, Magnon spin-current theory for

the longitudinal spin-Seebeck effect, Phys. Rev. B **89**, 014416 (2014).

[19] H. L. Wang, C. H. Du, Y. Pu, R. Adur, P. C. Hammel, and F. Y. Yang, Scaling of spin Hall angle in 3d, 4d, and 5d metals from $Y_3Fe_5O_{12}$/metal spin pumping, Phys. Rev. Lett. **112**, 197201 (2014).

[20] M. Kockert, R. Mitdank, A. Zykov, S. Kowarik, and S. F. Fischer, Absolute Seebeck coefficient of thin platinum films, J. Appl. Phys. **126**, 105106 (2019).

[21] J. Xu, J. He, J.-S. Zhou, D. Qu, S.-Y. Huang, and C. L. Chien, Electrical seebeck contrast observation of magnon Hall effect in topological ferromagnet $Lu_2V_2O_7$/heavy metal heterostructures, Phys. Rev. B **109**, L020401 (2024).

[22] J. Kimling, J. Gooth, and K. Nielsch, Anisotropic magnetothermal resistance in Ni nanowires, Phys. Rev. B **87**, 094409 (2013).

[23] L. Zhou, H. Song, K. Liu, Z. Luan, P. Wang, L. Sun, S. Jiang, H. Xiang, Y. Chen, J. Du, H. Ding, K. Xia, J. Xiao, and D. Wu, Observation of spin-orbit magnetoresistance in metallic thin films on magnetic insulators, Sci. Adv. **4**, eaao3318 (2018).

[24] H. Nakayama, M. Althammer, Y.-T. Chen, K. Uchida, Y. Kajiwara, D. Kikuchi, T. Ohtani, S. Geprägs, M. Opel, S. Takahashi, R. Gross, G. E. W. Bauer, S. T. B. Goennenwein, and E. Saitoh, Spin Hall magnetoresistance induced by a nonequilibrium proximity effect, Phys. Rev. Lett. **110**, 206601 (2013).

[25] X.-P. Zhang, F. S. Bergeret, and V. N. Golovach, Theory of spin Hall magnetoresistance from a microscopic perspective, Nano Lett. **19**, 6330 (2019).

[26] G. N. Grannemann and L. Berger, Magnon-drag Peltier effect in a Ni-Cu alloy, Phys. Rev. B **13**, 2072 (1976).

[27] M. E. Lucassen, C. H. Wong, R. A. Duine, and Y. Tserkovnyak, Spin-transfer mechanism for magnon-drag thermopower, Appl. Phys. Lett. **99**, 262506 (2011).

[28] S. J. Watzman, R. A. Duine, Y. Tserkovnyak, S. R. Boona, H. Jin, A. Prakash, Y. Zheng, and J. P. Heremans, Magnon-drag thermopower and Nernst coefficient in Fe, Co, and Ni, Phys. Rev. B **94**, 144407 (2016).

[29] M. V. Costache, G. Bridoux, I. Neumann, and S. O. Valenzuela, Magnon-drag thermopile, Nat. Mater. **11**, 199 (2012).

[30] T. Yamaguchi, H. Kohno, and R. A. Duine, Microscopic theory of magnon-drag electron flow in ferromagnetic metals, Phys. Rev. B **99**, 094425 (2019).

[31] G. Wang, L. Endicott, H. Chi, P. Lošt'ák, and C. Uher, Tuning the temperature domain of phonon drag in thin films by the choice of substrate, Phys. Rev. Lett. **111**, 046803 (2013).

[32] I. Pallecchi, F. Telesio, D. Marré, D. Li, S. Gariglio, J.-M. Triscone, and A. Filippetti, Large phonon-drag enhancement induced by narrow quantum confinement at the $LaAlO_3/SrTiO_3$ interface, Phys. Rev. B **93**, 195309 (2016).

[33] E. Erlandsen and A. Sudbø, Magnon drag in a metal–insulating antiferromagnet bilayer, Phys. Rev. B **105**, 184434 (2022).

[34] A. Ali Biswas and Y. Jana, Crystal-field, exchange interactions and magnetism in pyrochlore ferromagnet $R_2V_2O_7(R_{3+} = Y, lu)$, J. Magn. Magn. Mater. **329**, 118 (2013).

[35] A. Haghighirad, C. Gross, and W. Assmus, Powder synthesis and crystal growth of $Y_2V_2O_7$ under high pressure and its physical properties, J. Cryst. Growth **310**, 2277 (2008).

[36] H. J. Xiang, E. J. Kan, M.-H. Whangbo, C. Lee, S.-H. Wei, and X. G. Gong, Single-ion anisotropy, Dzyaloshinskii-Moriya interaction, and negative magnetoresistance of the spin-$\frac{1}{2}$ pyrochlore $R_2V_2O_7$, Phys. Rev. B **83**, 174402 (2011).

[37] M. Mena, R. S. Perry, T. G. Perring, M. D. Le, S. Guerrero, M. Storni, D. T. Adroja, C. Rüegg, and D. F. McMorrow, Spin-wave spectrum of the quantum ferromagnet on the pyrochlore lattice $Lu_2V_2O_7$, Phys. Rev. Lett. **113**, 047202 (2014).

[38] R. Matsumoto and S. Murakami, Rotational motion of magnons and the thermal Hall effect, Phys. Rev. B **84**, 184406 (2011).

[39] C. Moulsdale, P. A. Pantaleón, R. Carrillo-Bastos, and Y. Xian, Unconventional thermal magnon Hall effect in a ferromagnetic topological insulator, Phys. Rev. B **99**, 214424 (2019).

[40] A. Mook, J. Henk, and I. Mertig, Magnon Hall effect and topology in kagome lattices: A theoretical investigation, Phys. Rev. B **89**, 134409 (2014).

[41] M. Kockert, D. Kojda, R. Mitdank, A. Mogilatenko, Z. Wang, J. Ruhhammer, M. Kroener, P. Woias, and S. F. Fischer, Nanometrology: Absolute seebeck coefficient of individual silver nanowires, Sci. Rep. **9**, 20265 (2019).

[42] Tarachand, M. Saxena, B. Mukherjee, and G. S. Okram, A load-based thermopower measurement setup in the temperature range of 5–330 k, Rev. Sci. Instrum. **90**, 063904 (2019).

[43] L. S. Sharath Chandra, A. Lakhani, D. Jain, S. Pandya, P. N. Vishwakarma, M. Gangrade, and V. Ganesan, Simple and precise thermoelectric power measurement setup for different environments, Rev. Sci. Instrum. **79**, 103907 (2008).

[44] G. S. Okram, Intrinsic thermoelectric power of group vb metals, AIP Adv. **2**, 012178 (2012).

[45] S. J. Mason, A. Hojem, D. J. Wesenberg, A. D. Avery, and B. L. Zink, Determining absolute seebeck coefficients from relative thermopower measurements of thin films and nanostructures, J. Appl. Phys. **127**, 085101 (2020).

[46] K. Hoshi, T. Yamaguchi, A. Takeuchi, H. Kohno, and J.-i. Ohe, Magnon-drag thermoelectric transport with skyrmion structure, Appl. Phys. Lett. **117**, 062404 (2020).

[47] B. Flebus, R. A. Duine, and Y. Tserkovnyak, Landau-lifshitz theory of the magnon-drag thermopower, Europhys. Lett. **115**, 57004 (2016).

[48] A. D. Avery, R. Sultan, D. Bassett, D. Wei, and B. L. Zink, Thermopower and resistivity in ferromagnetic thin films near room temperature, Phys. Rev. B **83**, 100401(R) (2011).

[49] A. Prakash, J. Brangham, S. J. Watzman, F. Yang, and J. P. Heremans, Effect of magnons on interfacial phonon drag in YIG/metal systems, arXiv:1804.07023.

[50] J. Zhou, B. Liao, B. Qiu, S. Huberman, K. Esfarjani, M. S. Dresselhaus, and G. Chen, *Ab initio* optimization of phonon drag effect for lower-temperature thermoelectric energy conversion, Proc. Natl. Acad. Sci. USA **112**, 14777 (2015).

[51] P. Sheng, Y. Sakuraba, Y.-C. Lau, S. Takahashi, S. Mitani, and M. Hayashi, The spin nernst effect in tungsten, Sci. Adv. **3**, e1701503 (2017).